

Resonant Cavity Modes in $\text{Bi}_2\text{Sr}_2\text{CaCu}_2\text{O}_{8+x}$ Intrinsic Josephson Junction Stacks

Huili Zhang,¹ Raphael Wieland,² Wei Chen,¹ Olcay Kizilaslan,^{2,3} Shigeyuki Ishida,⁴ Chao Han,¹ Wanghao Tian,¹ Zuyu Xu,¹ Zaidong Qi,¹ Tong Qing,¹ Yangyang Lv,¹ Xianjing Zhou,¹ Nickolay Kinev,⁵ Andrey B. Ermakov,⁵ Eric Dorsch,² Marc Ziegele,² Dieter Koelle,² Hiroshi Eisaki,⁴ Yoshiyuki Yoshida,⁴ Valery P. Koshelets,⁵ Reinhold Kleiner,^{2,*} Huabing Wang,^{1,†} and Peiheng Wu¹

¹Research Institute of Superconductor Electronics, Nanjing University, Nanjing 210023, China

²Physikalisches Institut and Center for Quantum Science in LISA⁺, Universität Tübingen, D-72076 Tübingen, Germany

³Department of Biomedical Engineering, Faculty of Engineering, Inonu University, 44280 Malatya, Turkey

⁴Advanced Industrial Science and Technology, Electronics and Photonics Research Institute, Tsukuba 3058568, Japan

⁵Kotel'nikov Institute of Radio Engineering and Electronics, Moscow 125009, Russia

(Received 14 December 2018; revised manuscript received 8 February 2019; published 2 April 2019)

We report on a detailed investigation of terahertz-emission properties related to resonant cavity modes. We discuss data for an underdoped and an optimally doped $\text{Bi}_2\text{Sr}_2\text{CaCu}_2\text{O}_{8+x}$ (BSCCO) intrinsic junction stack having the same geometry. At high bias, in the presence of a hot spot, the emission frequency seems to be continuously tunable by changing the bias current and the bath temperature. By contrast, at low bias the emission frequencies f_e are remarkably discrete and temperature independent for both stacks. The values of f_e point to the formation of $(0, m)$ cavity modes with $m = 3$ to 6. The total voltage V across the stack varies much stronger than f_e , and there seems to be an excess voltage indicating groups of junctions that are unlocked. For the case of the underdoped stack we perform intensive numerical simulations based on coupled sine Gordon equations combined with heat-diffusion equations. Many overall features can be reproduced well and point to an unexpected large value of the in-plane resistivity. However, unlike in experiment, in simulations the different resonant modes strongly overlap. The reason for this discrepancy is presently unclear.

DOI: 10.1103/PhysRevApplied.11.044004

I. INTRODUCTION

Terahertz (THz) emitters consisting of stacks of intrinsic Josephson junctions (IJJs) made of the high-transition-temperature (high- T_c) cuprate $\text{Bi}_2\text{Sr}_2\text{CaCu}_2\text{O}_{8+\delta}$ (BSCCO) have attracted great interest in recent years, in terms of both experiment [1–50] and theory [51–83]. For recent reviews, see Refs. [84–86]. BSCCO is a layered superconductor with alternating superconducting and insulating sheets. A single crystal thus forms a natural stack of IJJs, with approximately 670 IJJs per μm of crystal thickness [87]. Due to the Josephson effect, in the resistive state the supercurrents across each IJJ oscillate with a frequency $f_J = V_J/\Phi_0$, where V_J is the voltage across the junction and Φ_0 is the flux quantum, $\Phi_0^{-1} = 483.6 \text{ GHz/mV}$. Assuming that the voltage drop across all N IJJs in the stack is the same, the Josephson relation can be written as $f_J = V/N\Phi_0$, where V is the total voltage

across the stack. Coherent off-chip terahertz emission was first demonstrated for 1- μm -thick BSCCO stacks, with an extrapolated output power up to $0.5 \mu\text{W}$ and emission frequencies f_e between 0.5 and 0.85 THz [1]. The emission frequency was found to be inversely proportional to the width of the stack, leading to the conclusion that resonant cavity modes oscillating along the width of the stack play an important role in synchronization. A variety of cavity resonances have indeed been found and analyzed [2–4,6,8,9,12,25,41,49,53,62,63,67,74,80–82]. For a rectangular stack of length L and width W the cavity modes can exhibit m half waves along the length and p half waves along the width, and the resonance frequencies of these modes are given by $f_c = c_1 \sqrt{(p/2W)^2 + (m/2L)^2}$, with the in-phase mode velocity c_1 . At low temperatures and for very thick stacks $c_1 \approx 7 \times 10^7 \text{ m/s}$. The expression for f_c implicitly assumes that the cavity modes are well defined (i.e., have a high quality-factor). The expression also assumes that the whole stack is superconducting and at a roughly constant temperature.

There are in fact two emission regimes for IJJ stacks, which can roughly be distinguished from the shape of

*kleiner@uni-tuebingen.de

†hbwang@nju.edu.cn

the current-voltage characteristics (IVCs). Since the out-of-plane resistivity of BSCCO decreases with increasing temperature, the IVCs exhibit a positive differential resistance at low currents but start to backbend at larger currents and the differential resistance becomes negative. At moderate input power (“low-bias regime”), Joule heating is small and the temperature distribution in the stack is almost homogeneous and close to the bath temperature T_b . By contrast, in the “high-bias regime” the current and temperature distributions in the stack become strongly nonuniform and a hot spot—i.e., a region with a temperature above T_c —forms [3,6,8,15,21,24,33,35,64,72]. The hot spot grows in size with increasing current and can coexist with regions that are still superconducting and produce terahertz radiation. In the presence of the hot spot, one can still detect standing-wave patterns outside the hot-spot region [3,6,8]. However, the size of the cold part of the stack varies as a function of bias current and bath temperature, and the geometric boundary conditions are no longer purely fixed by the geometry of the stack. The emission frequency becomes tunable [33,35,36]. Interestingly, the linewidth of radiation is much lower in the presence of the hot spot [14]. However, many samples do not emit in the high-bias region, and the reason for this is unclear.

There are, thus, many unresolved issues about THz emission and standing-wave formation, asking for a detailed study over a wide range of bias conditions and possibly a close comparison to numerical simulations. We perform such a study using two intrinsic Josephson junction stacks of the same geometry and a junction number of about 700. The stacks are fabricated, respectively, from an underdoped and an optimally doped BSCCO single crystal. Both stacks emit in the low-bias regime. At high bias only the optimally doped stack emits THz radiation. For this stack, at high bias the emission frequency is continuously tunable by changing the bias current and the bath temperature, and all IJJs seem to be synchronized. By contrast, at low bias the emission frequencies f_e are remarkably discrete and similar for both stacks, pointing to the excitation of $(0, m)$ cavity modes with $m = 3$ to 6. Surprisingly, the total voltage V across the stack varies much stronger than f_e , and there seems to be an excess voltage indicating groups of junctions that are unlocked. For the case of the underdoped stack we also perform intensive numerical simulations based on coupled sine Gordon equations combined with heat-diffusion equations [77,78,83]. Many features, like the shape of the current-voltage characteristics, the absence of high-bias emission, or the temperature and voltage regions where emission occurs at low bias, can be reproduced and point to an unexpected large value of the in-plane resistivity. However, in our simulations the different resonant modes strongly overlap for realistic model parameters. The pronounced discreteness of the experimentally observed emission frequencies remains

unclear. We finally note that also in simulations the emission frequency in the high-bias regime—as far as there was emission at all—turned out to be continuous in good agreement with experiment.

II. SAMPLES AND EXPERIMENTAL TECHNIQUES

We perform our measurements on stand-alone BSCCO stacks embedded between gold electrodes, so-called gold-BSCCO-gold (GBG) structures. The inset in Fig. 1 shows a sketch of the geometry. The preparation of the sample is described in detail in Ref. [26]. In brief, a BSCCO single crystal is glued onto a silicon substrate with polyimide. A 100-nm-thick gold film is deposited on the crystal immediately after cleaving. As the third step, a $400 \times 200 \mu\text{m}^2$ wide rectangular mesa is fabricated using photolithography. The thickness of the mesa is about $1.2 \mu\text{m}$. The sample is then glued to a MgO substrate using polyimide. The base crystal is cleaved away by removing the silicon substrate, leaving the mesa standing alone surrounded by polyimide. The fresh surface is immediately covered with a 100-nm-thick gold layer. Photoresist is patterned in a rectangular, a $300 \times 50 \mu\text{m}^2$ -wide area over the cleaved mesa using photolithography, and then the whole sample is etched down to the bottom gold layer by ion milling, resulting in a nominally (within about $\pm 10\%$ accuracy) $1.2\text{-}\mu\text{m}$ -thick stand-alone stack with lateral dimensions of $300 \times 50 \mu\text{m}^2$ contacted by the top and bottom gold layers. The nominal thickness of the stack corresponds to about 800 IJJs. In this paper, data of two samples are presented. Sample 1 is fabricated from an Ar-annealed underdoped BSCCO single crystal with $T_c \approx 76$ K. Sample 2 is fabricated from an as-grown BSCCO single crystal near optimal doping with $T_c \approx 89$ K. The samples are

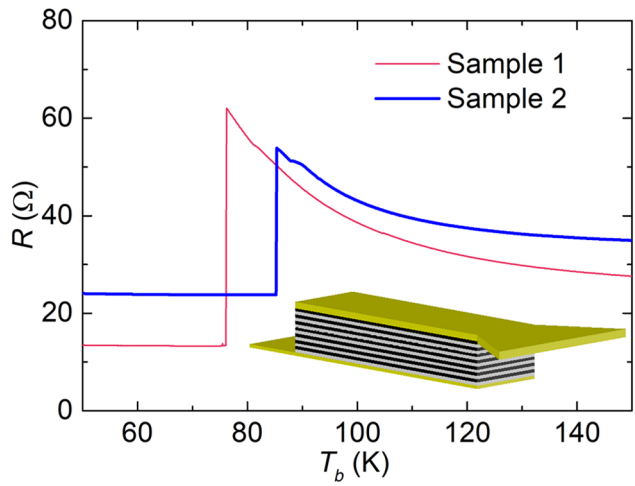


FIG. 1. Resistance of the BSCCO stacks sample 1 (thin line) and sample 2 (thick line) vs bath temperature T_b . Inset shows a sketch of the stacks.

mounted separately onto hemispherical silicon lenses 6 mm in diameter and placed into a Stirling cooler, which can cool down to 27.8 K from room temperature. The THz radiation is focused by the lens, then transmitted outward through a homemade Fourier-transform infrared spectrometer and is finally detected by a Golay cell. The IVCs, the THz emission power P_e , and frequency-resolved spectra determining the emission frequency f_e can be measured simultaneously. The power-detection and frequency measurements are similar to our previous studies [6].

Figure 1 shows the dependence of the c -axis resistance of the two samples on bath temperature T_b . Below T_c nearly temperature-independent contact resistances of 13.5 and 23.5 Ω are observed for samples 1 and 2, respectively. About 9 Ω (sample 1) and 13 Ω (sample 2) arise from the resistance between the BSCCO stacks and the contacting Au layers, the remaining resistance is due to the wiring scheme. The contact resistances are subtracted from the measurements discussed below.

III. RESULTS

To introduce our transport and emission measurements, Fig. 2 shows data for sample 2, taken at $T_b = 55$ K. The inset in (a) shows the IVC, measured for currents between 0 and 40 mA. For this and other recordings of IVCs addressed below we ramp up the current from zero to some

maximum value and then decrease the current back to zero. In the IVC shown in Fig. 2(a), upon increasing current, the stack switches at $I = 33$ mA from the zero-voltage state to an intermediate state where some groups of junctions are resistive and finally, at $I = 35$ mA, it switches to a state where all junctions in the stack are resistive. When the current is decreased, all IJJs remain in their resistive state until, for currents below 6.5 mA, some junctions and finally all of them return to the zero-voltage state. The THz-emission power P_e is bolometrically detected simultaneously to the IVC recording and plotted in Fig. 2(b) vs bias current. Upon decreasing current, the sample starts to emit at currents below 22 mA and displays a shallow emission maximum near $I = 17$ mA and $V = 0.88$ V, i.e., near the maximum voltage in the IVC. There is a stronger emission maximum at a current of about 9 mA. We next take THz-emission spectra at several bias points. 18 of them, recorded at the bias points indicated by circles in Figs. 2(a) and 2(b), are displayed in Fig. 2(c). For the spectra (1) to (9) there is only a single emission peak with power P_e at frequency f_e , which slightly shifts to lower-frequency values when decreasing the bias current. The linewidth of the peaks of roughly 7.5 GHz is given by the frequency resolution of our spectrometer. For each spectrum, f_e and the voltage V are indicated in the graphs. From the relation $f_e = V/N\Phi_0$ we deduce a junction number of $N = 705 \pm 5$ in this regime. For spectra (10) to (13), which

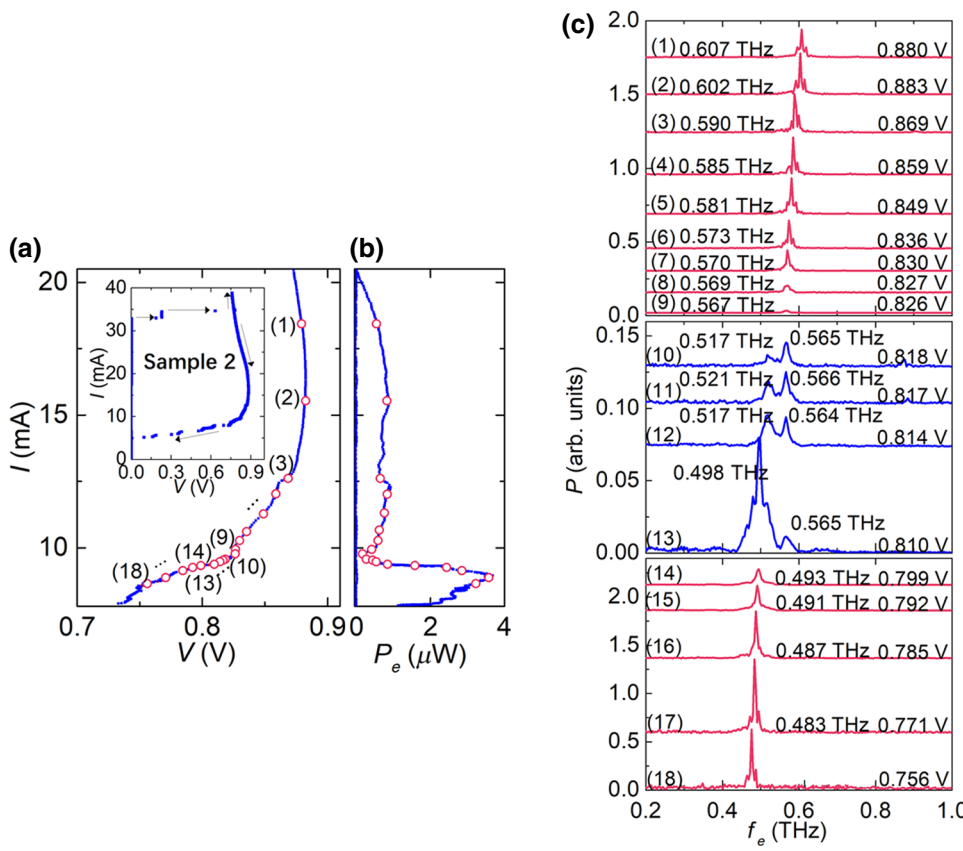


FIG. 2. For sample 2, (a) IVC at $T_b = 55$ K on a large current and voltage scale (inset) and on enlarged scales (main graph) near the voltage maximum. (b) THz-emission power P_e vs bias current. Graphs (c) show 18-THz emission spectra at bias points indicated by circles in (a) and (b). The spectra are vertically offset for clarity. Numbers in the graphs indicate the emission frequencies (peaks in the emission spectra) f_e and the voltage V across the stack. Note the enlarged power scale for spectra (10) to (13). Arrows in the inset in (a) indicate the direction of current sweep.

are taken near the minimum in P_e vs I in Fig. 2(b) we find two emission peaks located near 0.565 and 0.517 THz. This implies that either the stack switches between the two oscillation frequencies in time or it has grouped the IJJs into (at least) two regions along the z axis where the junctions oscillate at different frequencies at the same time and thus develop different dc voltages. When decreasing the current further the lower-in-frequency peak survives and shifts to lower values of f_e , cf. spectra (14) to (18). For this low-frequency peak we would infer values of N between 785 and 770, the value decreasing with decreasing current. We thus see that, at least for the data taken at $T_b = 55$ K, the emission frequency varies in an almost discrete way, with an unclear junction number inferred from the total voltage V .

To address this in more detail we next show in Figs. 3(a) and 4(a) families of IVCs taken at bath temperatures between 28 and 70 K. Figure 3(a) is for sample 1 and

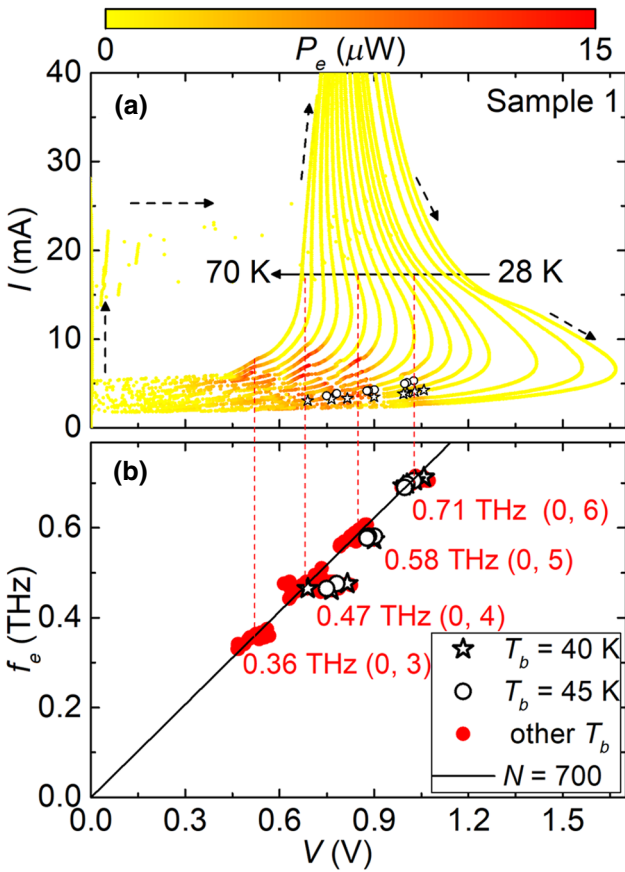


FIG. 3. For sample 1, (a) IVCs at different temperatures T_b (28, 30, 35 K and from 40 to 70 K in steps of 2.5 K). The color code indicates the emission power P_e . (b) Emission frequency f_e vs voltage V across the stack for all bath temperatures. The solid line corresponds to $V = Nf_e\Phi_0$ with $N = 700$. The asterisks and open circles represent the selected bias points to measure f_e for $T_b = 40$ K and $T_b = 45$ K, respectively. Dashed arrows in (a) indicate the direction of the current sweep.

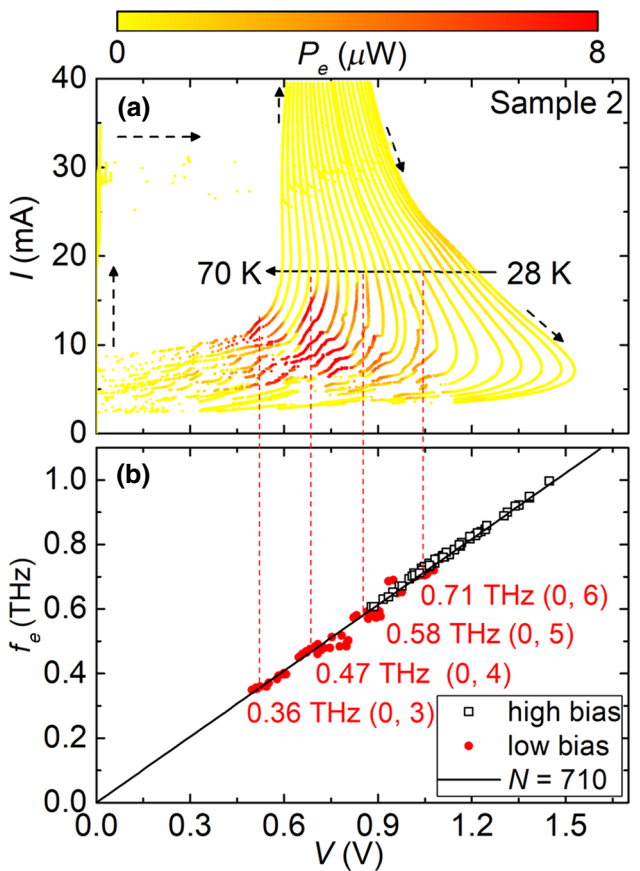


FIG. 4. For sample 2, (a) IVCs at different temperatures T_b from 28 to 70 K in steps of 2 K. The color code indicates the emission power P_e . (b) Emission frequency f_e vs voltage V across the stack for all bath temperatures. The solid line corresponds to $V = Nf_e\Phi_0$ with $N = 710$. Dashed arrows in (a) indicate the direction of the current sweep.

Fig. 4(a) sample 2. Each IVC is recorded as described for Fig. 2. For sample 1, THz emission, displayed by the color scale in Fig. 3(a), is only detectable in the low-bias regime where the differential resistance in the IVC is positive. The maximum voltage where emission occurs is about 1.1 V and the current range where emission is seen is between 2 and 10 mA. The emitting region seems to be weakly modulated in roughly vertical stripes, a feature that has been seen in the past [27,32,41,77] and is attributed to the formation of different standing waves being excited in the stack.

Figure 3(b) shows emission frequencies f_e , inferred from a large number of spectra, vs the total voltage V across the stack. The scatter of the data points along the frequency axis is much less than the scatter along the voltage axis and one clearly observes four discrete emission frequencies near 0.36, 0.47, 0.58, and 0.71 THz. These values indicate that (0,3), (0,4), (0,5), and (0,6) resonances have formed in the stack under the various bias conditions. Unfortunately, the contacting Au layers are too thick (100 nm) to perform low-temperature scanning laser

microscope measurements, which are usually done using Au thicknesses of 30 nm or less. However, we note here, that for our geometry the resonance frequencies of $(1, m)$ modes—such modes are usually considered for strong radiation—would be 720 GHz or higher, with the exception of $m = 0$, which is degenerate with the $(0, 6)$ mode. However, the fact that the emission power observed near 710 GHz is not very large is in contrast to the expectation that the $(1, 0)$ mode radiates stronger than $(0, m)$ modes. Thus, unless one invokes higher modes associated with mode velocities $c_q \approx c_1/q$ ($q = 2, 3, 4$, etc.), only the modes $(0, 3)$, $(0, 4)$, $(0, 5)$, and $(0, 6)$ are compatible with the data. For the mode velocity $c_1 = 2Lf_e/m$, m being the mode index and $L = 600 \mu\text{m}$ being the length of the stack, we find a value of $7.1 \times 10^7 \text{ m/s}$, which is consistent with previous measurements [16,85]. The solid line in Fig. 3(b) is given by the function $f_e = V/N\Phi_0$, with $N = 700$ being (approximately) the total number of IJJs in the stack. While a large number of data points is located on or at least near this line, some of the data points are clearly located at higher voltages, and some are located at lower voltages. Data points left of the solid line can be explained naturally by assuming that some of the junctions in the stack have switched back to the zero-voltage states. In simulations, cf. Sec. IV, we find that a number of junctions being located at the top or the bottom of the stack are not locked to the resonance that has formed, but have developed a higher dc voltage. In these simulations, the total voltage across the stack can exceed by more than 10% the voltage expected for all junctions being locked. This seems to be a natural explanation for the spread in V . We further note that between the regions where different resonances occur the IVCs exhibit jumps and sometimes changes of slope. If all junctions of the stack were locked to a given resonance one would expect a step (an upturn) in the IVC with low differential resistance. If, however, at the same time the number of locked junctions varies, the shape of such steps could become very complicated, like observed for sample 1. For clarity, in Fig. 3 we have marked some of the subsequent spectra taken at bath temperatures of, respectively, 40 and 45 K with asterisks and open circles. One observes a tendency that, when the emission frequency has jumped toward a lower value while decreasing the bias current, the voltage is larger than expected for the resonance, while before the jump it is close to the value expected for all junctions being locked. This goes in line with the data discussed in Fig. 2 and indicates that transitions to lower-index resonances occur when the point of strongest phase lock is exceeded.

Figure 4(a) shows families of IVCs for sample 2. In spite of the very different doping state of this sample compared to sample 1, the overall shape of the IVCs is very similar to the ones shown in Fig. 3(a), indicating that the (subgap) resistance and the thermal parameters of both samples are not too different. In contrast to sample 1, sample 2 also

emits in the high-bias regime, i.e., in the presence of a hot spot, although with low emission power. At low bias the appearance of stripelike modulations of the emitted THz power is less evident than for sample 1. Still in a plot of f_e vs V , cf. Fig. 4(b), one observes discrete values for the emission frequencies in the low-bias regime (solid circles), which are very close to the frequency values observed for sample 1. By contrast, in the high-bias regime (open squares) the emission frequencies seem to vary continuously. This is also a feature that has been observed many times before; it can be attributed to the fact that the hot spot (and thus also the cold region) can have variable sizes and positions. The solid line in Fig. 4(b) is given by the function $f_e = V/N\Phi_0$, with $N = 710$. The high-bias data are located very close to this line whereas, like for sample 1, in the low-bias regime some data points are significantly shifted towards the right of the line. Further note that the emission frequencies observed in Fig. 2 would correspond to a transition between the $(0, 5)$ and the $(0, 4)$ mode.

To further evaluate our data we show, for sample 1 in Fig. 5(a), emission frequencies vs bath temperature and in Fig. 5(b) the emission power vs emission frequencies. Color scales in (a) and (b) denote emission power and bath temperature, respectively. In both plots, the discreteness of the values of f_e is evident and, in addition, from Fig. 5(a) it is seen from the temperature independence of the resonant frequencies, that the mode velocity c_1 is basically temperature independent. This result is surprising, because from coupled sine-Gordon equations one expects c_1 to decrease with temperature and even approach zero for $T_b \rightarrow T_c$. The reason is the decrease in Cooper-pair density with increasing temperature, resulting in an increase and for $T_b \rightarrow T_c$ the divergence of the kinetic inductance associated with supercurrent flow. In fact, in Ref. [34] the decrease of the emission frequency with bath temperature was reported for two mesa structures. By contrast, for a stand-alone stack the emission frequency was also found to be temperature independent. We will address this further in Sec. IV.

For sample 2, Fig. 6 shows (a) f_e vs T_b and (b), (c) P_e vs f_e . For this sample, emission was detectable both in the presence of a hot spot (square symbols) and at low bias (circles). Both plots confirm that in the high-bias regime the emission frequency varies continuously, while at low bias the emission frequencies are discrete and, as far as detectable, independent of T_b .

IV. COMPARISON TO SIMULATIONS

Our simulations are based on coupled sine-Gordon equations combined with heat-diffusion equations, as described in detail in Refs. [77,78,83]. In these simulations hot-spot formation is included, as well as the appearance of standing electromagnetic waves. These waves are in fact accompanied by the formation of almost static columns of

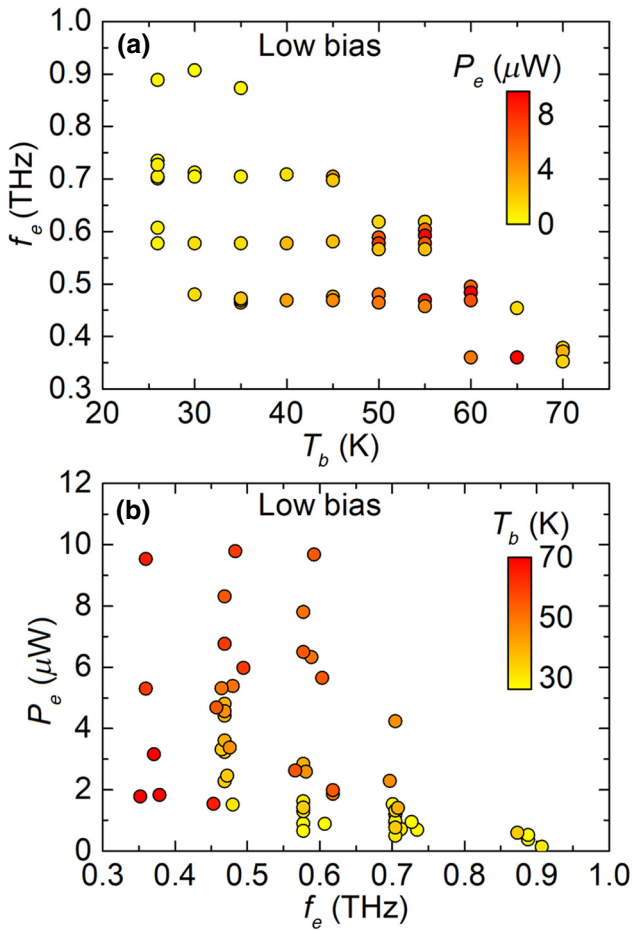


FIG. 5. For sample 1, (a) emission frequency f_e vs bath temperature T_b over a large temperature range up to 70 K. The color code indicates the emission power P_e . (b) Emission power P_e vs emission frequency f_e at various T_b values indicated by the color code. [52–54].

Josephson fluxons and antifluxons [77,78], as predicted in Refs. [52–54].

In the model, the electrical and thermal model parameters depend on temperature, and thus, for an inhomogeneous temperature distribution, on coordinates x , y , and z . Their spatial variation, as well as $T(x, y, z)$, are found self-consistently by solving the thermal equations (requiring Joule heat dissipation as an input from the electric circuit) and the electrical equations (requiring the temperature distribution in the stack, as determined from the thermal circuit). In the present paper we consider a stand-alone IJJ stack, with $T_c = 75$ K, consisting of $N = 700$ IJJs. These parameters are not too far from those of sample 1. The rectangular stack has a length $L_s = 300 \mu\text{m}$ along x and a width $W_s = 50 \mu\text{m}$ along y . It is covered by two gold layers and cooled from the bottom side. The bottom of the substrate is kept at bath temperature T_b . We assume that between the substrate and the BSCCO stack there is a layer with poor thermal conductivity κ_g and thickness d_g , which

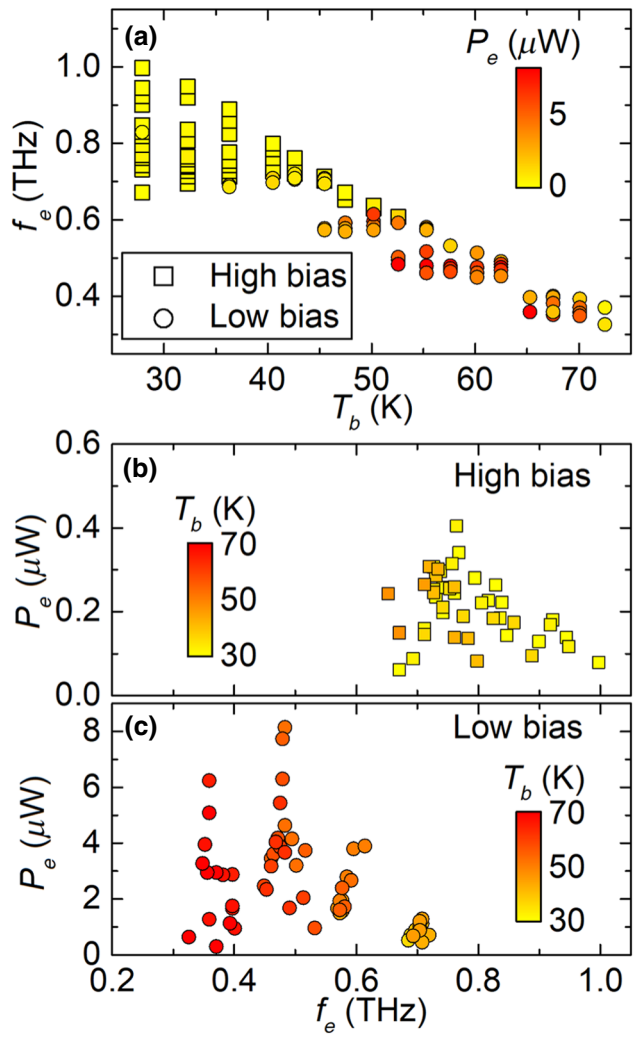


FIG. 6. For sample 2, (a) emission frequency f_e vs bath temperature T_b over a large temperature range up to 70 K. The color code indicates the emission power P_e . (b) and (c) show emission power P_e at high bias and low bias, respectively, vs emission frequency f_e at various T_b values indicated by the color code.

we use as a fit parameter to roughly match the $T_b = 28$ K IVC to the experimental curve. For the simulations presented we take $d_g = 30 \mu\text{m}$ and $\kappa_g = 1 \text{ W/mK}$. We further assume for the thermal description that the IJJ stack plus the contacting Au layer have a temperature $T_m(x, y)$, which is constant along z but can vary along x and y . For the BSCCO thermal conductivity we use the same values and temperature dependences as in Ref. [83]. In z direction the substrate (thickness 100 μm , thermal conductivity 1000 W/mK) is discretized by two segments, and each poorly conducting sheet by nine segments. For this geometry, we solve the heat-diffusion equation $c dT/dt = \nabla(\kappa \nabla T) + q_s$, with the specific heat capacity c , the (anisotropic and layer dependent) thermal conductivity κ , and the power density q_s for heat generation in the stack.

For the electric circuit we group the N IJJs in the stack to $M = 50$ segments, each containing $G = N/M = 16$ IJJs, assumed to have identical properties. G explicitly appears in the electrodynamic equations and leads to well-behaved scaling, i.e., in particular, in-phase dynamic solutions appear almost independent of the choice of M , provided that M is sufficiently large.

In the model the electric current density j_{ext} is injected into the Au layer, which we assume to have a low enough resistance to freely distribute the current before it enters the IJJ stack in z direction with a density $j_{z,\text{Au}}$ proportional to the local BSCCO conductance $\sigma_c(x,y) = \rho_c^{-1}(x,y)$. The full expression is $j_{z,\text{Au}} = \langle j_{\text{ext}} \rangle \sigma_c(x,y) / \langle \sigma_c \rangle$, the brackets denoting spatial averaging. The same current leaves the lower Au electrode. We solve sine-Gordon-like equations for the Josephson phase differences $\gamma_l(x,y)$ in the l th segment of the IJJ stack:

$$\begin{aligned} Gsd_s \nabla \left(\frac{\nabla \dot{\gamma}_l}{\rho_{ab}} \right) + G\lambda_k^2 \nabla(n_s \nabla \gamma_l) \\ = \left(2 + \frac{G^2 \lambda_k^2 n_s}{\lambda_c^2} \right) j_{z,l} - j_{z,l+1} - j_{z,l-1}. \end{aligned} \quad (1)$$

Here, $l = 1 \dots M$, $\nabla = (\partial/\partial x, \partial/\partial y)$, $d_s = 0.5$ nm is the thickness of the superconducting layers and $\lambda_k = [\Phi_0 d_s / (2\pi \mu_0 j_{c0} \lambda_{ab0}^2)]^{1/2}$, with the in-plane London penetration depth λ_{ab0} and the magnetic permeability μ_0 . $\lambda_c = [\Phi_0 / (2\pi \mu_0 j_{c0} s)]^{1/2}$ is the out-of-plane penetration depth. Time is normalized to $\Phi_0 / 2\pi j_{c0} \rho_{c0} s$, resistivities to ρ_{c0} and current densities to j_{c0} .

The z -axis currents consist of Josephson currents with critical current density $j_c(x,y)$, (ohmic) quasiparticle currents with resistivity $\rho_c(x,y)$ and displacement currents with (temperature-independent) dielectric constant ε . One obtains

$$j_{z,l} = \frac{\beta_{c0}}{G} \ddot{\gamma}_l + \frac{\dot{\gamma}_l}{\rho_{c,l}} + j_c \sin(\gamma_l) + j_{z,l}^N, \quad (2)$$

with $\beta_{c0} = 2\pi j_{c0} \rho_{c0}^2 \varepsilon \varepsilon_0 s / \Phi_0$; $s = 1.5$ nm is the interlayer period, ε_0 is the vacuum permittivity, and the $j_{z,l}^N$ are the out-of-plane noise current densities. The in-plane current densities are calculated as in Refs. [78,83]. For the electrical parameters we use the 4.2-K values $\rho_{c0} = 1550 \Omega$ cm, $j_{c0} = 250 \text{ A/cm}^2$, $\lambda_{ab0} = 260$ nm, and $\varepsilon = 9$, yielding $\lambda_c = 264 \mu\text{m}$, $\lambda_k = 0.88 \mu\text{m}$, and $\beta_{c0} = 2.18 \times 10^5$. For the temperature dependence of j_c we use a parabolic profile, $j_c \propto 1 - (T/T_c)^2$; for the temperature dependence of ρ_c see Ref. [77].

The choice of $\rho_{ab}(T)$ requires some discussion. In general, $\rho_{ab}(T)$ (like other model parameters also) is a function of both temperature, frequency, and the doping state of the BSCCO crystal. Since we cannot implement this fully in our model we focus on the relevant frequency range

between 0.3 and 0.7 THz and temperatures above 25 K and we approximate $\rho_{ab}(T)$ by σ_1^{-1} , where $\sigma_1(T)$ is the real part of the in-plane microwave conductivity. $\sigma_1(T)$ exhibits a shallow maximum below T_c , and consequently $\rho_{ab}(T)$ has a minimum at this temperature. We found through many simulations that our results depend critically on this minimum value. For the present simulations we use the results of Ref. [88] for $\sigma_1(T)$, where in the frequency range between 0.3 and 0.7 THz $\sigma_1(T)$ is found to vary in the range $(0.7 - 1.7) \times 10^6 \Omega^{-1}\text{m}^{-1}$. We approximate this $\sigma_1(T)$ by a parabolic temperature dependence below T_c continuing $\propto T^{-1}$ for temperatures above T_c . For the minimum $\rho_{ab,\min}$ at $T = 50$ K, taking into account that in our model only slabs (the CuO₂ layers) of 0.3-nm thickness are conducting, one expects values in the range $(12 - 29) \mu\Omega$ cm. For $12 \mu\Omega$ cm it turns out the stack dynamics is too strongly damped. Below we thus show results for $\rho_{ab,\min}$ values of 20 and $30 \mu\Omega$ cm, which still seems to be too low to explain all features found experimentally.

We also study two types of boundary conditions with respect to j_z . In our standard simulations we approximate the current densities leaving the stack by the (time-independent) applied current density, as described above. For these conditions, all high-frequency components generated by the Josephson effect are confined in the stack. Below, this is referred to as boundary condition 0 (BC = 0). To allow ac currents to flow into the Au layer we now also consider a configuration where we explicitly include the Au layers, modeled as ideal conductors. These layers are separated from the actual stack by a “dead layer” of thickness d_d mimicking the contact resistance of the sample. In the simulation discussed below d_d is set to 30 nm and for the contact resistance $\rho_c(T)$ of the BSCCO stack is used. This boundary condition is referred to as boundary condition 1 (BC = 1). It in fact turned out during the simulations done for the present paper that BC = 1 has a similar effect as using BC = 0 with a reduced value of $\rho_{ab,\min}$. In other words, the Au layer, as we included here acts like an additional damping element.

In an initial sequence of simulations we discretized the stack using 50 grid points along x and 10 grid points along y and calculated IVCs for different bath temperatures. In these simulations we always found $(0, m)$ cavity modes. We thus restricted ourselves to a 2D configuration, using only one grid point along y for further calculations.

A fifth-order Runge-Kutta scheme is used to evolve the above equations in time. For a given set of input parameters, in a first initializing step we solve the heat-diffusion equation considering dissipation by out-of-plane quasiparticle currents only, in order to achieve stationary distributions for the temperature and j_{ext} . Then, in a second initializing step, heat-diffusion and sine-Gordon equations are solved simultaneously over typically 5000 Josephson oscillations. In most simulations we start with

constant phases $\gamma_l = 0$ and evolve the dynamics over time. In some cases we trigger solutions, by using cosine profiles for γ_l , alternating between adjacent layers. This triggers fluxon-antifluxon rows. Further, all simulations are initialized in a state where all junctions are resistive, by using proper initial conditions for the $\dot{\gamma}_l$. After the initialization steps various quantities, partially averaged over spatial coordinates, are tracked as a function of time to produce time averages or to make Fourier transforms. In particular, we calculate spatially resolved time averages of the power $\langle q(x) \rangle$ dissipated by in-plane currents [77], as well as Fourier transforms of the integrated power $q_{||}$ dissipated by in-plane currents oscillating at the Josephson frequency. $\langle q(x) \rangle$ has turned out to be an effective quantity to identify resonant modes while $q_{||}$ serves as a surrogate for the emitted radiation for which we have no direct numerical access in our simulations.

Figures 7(a)–7(c) show simulated families of IVCs for different bath temperatures and three sets of parameters: (a) boundary condition 0 and $\rho_{ab,\min} = 30 \mu\Omega \text{ cm}$, (b) boundary condition 0 and $\rho_{ab,\min} = 20 \mu\Omega \text{ cm}$, and (c) boundary condition 1 and $\rho_{ab,\min} = 30 \mu\Omega \text{ cm}$.

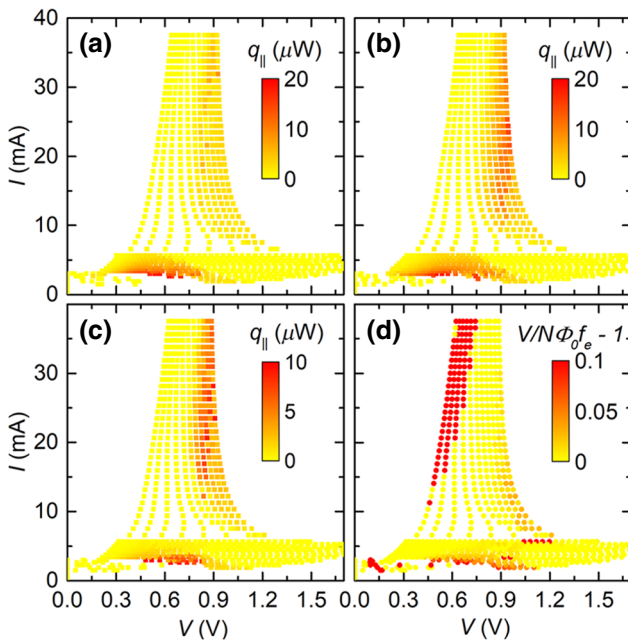


FIG. 7. Simulated families of IVCs for different bath temperatures using (a) boundary condition 0 and $\rho_{ab,\min} = 30 \mu\Omega \text{ cm}$, (b) boundary condition 0 and $\rho_{ab,\min} = 20 \mu\Omega \text{ cm}$, and (c) boundary condition 1 and $\rho_{ab,\min} = 30 \mu\Omega \text{ cm}$. For currents between 5.6 and 37.5 mA IVCs are displayed for bath temperatures between 28 and 68 K, with a temperature step of 4 K between adjacent curves. For currents below 5.6 mA the bath temperature varies between 28 and 71 K and the temperature step between adjacent curves is 1 K. The color scale indicates the power $q_{||}$ dissipated by in-plane currents oscillating at the Josephson frequency. Graph (d) is based on the current and voltage data of graph (c) and uses the relative excess voltage $V/N\Phi_0f_e - 1$ as the color scale.

boundary condition 1 and $\rho_{ab,\min} = 30 \mu\Omega \text{ cm}$. All other model parameters are the same for the three graphs. The color scale indicates the power $q_{||}$ dissipated by in-plane currents oscillating at the Josephson frequency.

The overall shape of the calculated IVCs at a given bath temperature is nearly the same for all three graphs and it is not too far from the experimental IVCs shown in Fig. 3. In the simulated curves, the high-bias regime, where a hot spot has formed, starts at currents above about 7 mA. In this high-bias regime, the values for $q_{||}$ are very small in Fig. 7(a). Only in a few points $q_{||}$ is on the order of 5 μW . In contrast, in Figs. 7(b) and 7(c) one observes an “emitting” regime at high bias. Here, as well as in many other simulations of IJJ stacks we observe that the emission frequency varies continuously, in agreement with experimental data. With respect to the observability of emission it in fact has turned out during many simulations, that for high in-plane damping (low values of $\rho_{ab,\min}$) standing-wave formation is robust in the presence of a hot spot. For increasing values of $\rho_{ab,\min}$, the stack becomes increasingly more unstable against the formation of out-of-phase modes or disordered phase distributions, resulting in a loss of in-phase resonant modes. The precise value of $\rho_{ab,\min}$ depends on the other model parameters and on the boundary condition used, cf. Fig. 7(c), but in most cases requires values well above 20 $\mu\Omega \text{ cm}$, which is on the upper limit of the values expected from microwave conductivity measurements. We have further seen in other simulations that in the high-bias regime the formation of collective resonant modes becomes unstable under the effect of vertical gradients in junction parameters, e.g., the out-of-plane resistance. This may also contribute to the nonobservability of the high-bias emission for some samples.

In the low-bias regime, the temperature variation in the stack is smooth, exhibiting a parabolic shape with a maximum in the center of the stack, which is typically 2–3 K above bath temperature. In this regime we cannot find standing waves at high voltages, e.g., above 1.2 V for the curves shown in Figs. 7(a)–7(c). Even triggered waves die out in this regime. Standing waves, leading to large values of $q_{||}$, are observed for voltages between 0.3 and 1.1 V (0.43–1.57 mV per junction) and for currents below about 6 mA. In this regime different $(0, m)$ modes are excited, with m between 3 and 7. The overall shape of the region where resonances have formed resembles the emitting region in the experimental data, although the current and voltage ranges, where sample 1 emits, are somewhat larger than in simulation. Different from experiment, however, the calculated data look smooth and do not exhibit a striplike modulation.

Let us turn to a more detailed discussion of the low-bias regime. In experiment it has been seen that the voltage V across the stack can exceed by around 10% the voltage expected from the Josephson relation when all junctions are locked to some resonant mode. To investigate this in

our simulations we plot the quantity $V/N\Phi_0f_e - 1$, yielding the relative excess voltage compared to the case when all junctions are locked to a resonance, for a large number of data points. The result is shown in Fig. 7(d) for the IVC families plotted in Fig. 7(c). We observe an excess voltage of up to 10% in the region of strong low-bias emission. Another region with excess voltages in the 2% range appears at high bias, in a region where $q_{||}$ is relatively low. Except for this region the excess voltage at high bias is almost zero.

To address the excess voltage in the low-bias regime further, we plot in Fig. 8(a) the low-bias part of the IVC at $T_b = 47$ K and in Fig. 8(b) we plot for selected normalized bias currents the segment-resolved voltage per junction vs the segment index l (running from 1 to 50). In (a) the color scale is given by $q_{||}$. For currents between 3.5 and 2.6 mA an $m = 5$ mode has developed in the stack. One notes in Fig. 8(a) that the maximum value of $q_{||}$ is reached at the very end of the resistive branch, i.e., right before large groups of junctions switch back to the zero-voltage state. One further notes that in the current range between 3.66 and 2.72 mA, where the $m = 5$ mode has formed, the slope of the IVC is almost linear, a feature that can at least sometimes be seen in the experimental IVCs. In this current range, with decreasing current, the excess voltage increases from 2.1% to 8.2%. For the lowest bias point in the fully resistive state, exhibiting the highest value of $q_{||}$, the excess voltage is even larger, 13%.

The curves in Fig. 8(b) are an indicator of which parts of the stack are locked to the resonant mode (for phase-locked segments, the voltages V_l are identical). For a normalized current I/I_{c0} of 0.1 ($I_{c0} = 37.5$ mA) the $m = 5$ resonance has not yet developed. The resonance develops at lower current values, however only the inner segments of the stack are locked to the resonance while the voltage across

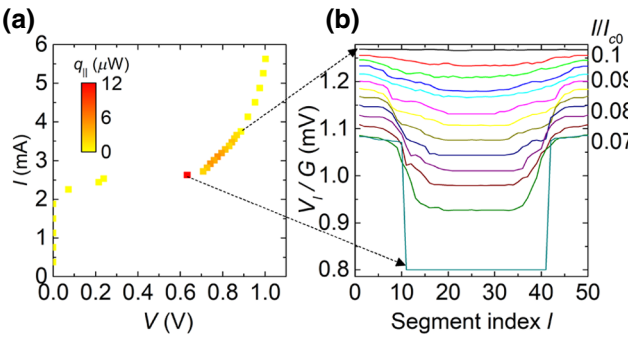


FIG. 8. For the model parameters of Fig. 7(c), (a) low-bias part of the IVC at $T_b = 47$ K and (b) segment-resolved voltages per junction V_k/G vs segment index l for normalized bias currents I/I_{c0} between 0.1 and 0.07 in steps of 0.025, with $I_{c0} = 37.5$ mA. The color scale in (a) indicates the power $q_{||}$. Arrows from (a) to (b) indicate the two outermost bias points in the IVC for which V_k/G is shown in (b).

the segments located near the top and bottom part of the stack is higher, i.e., Josephson currents in these segments oscillate at higher frequencies. With decreasing current, the number of locked segments increases, however even for $I/I_{c0} = 0.07$, the bias for which $q_{||}$ is highest, the phase lock is incomplete and consequently there is a positive excess voltage.

Another important experimental observation was the clear discreteness of the resonant frequencies, cf. Fig. 5. This is clearly different from our simulations where the resonant modes seem to strongly overlap. To investigate this more clearly we trigger resonant modes between $m = 3$ and $m = 6$ for a fixed normalized current $I/I_{c0} = 0.1$ and vary the bath temperature to change the voltage across the stack and also the resonant frequency. Results are shown in Figs. 9(a)–9(c) where we plot $q_{||}$ vs the “emission frequency” f_e . The graphs are for different model parameters, (a) boundary condition 0 and $\rho_{ab,\min} = 30 \mu\Omega \text{ cm}$, (b) boundary condition 0 and $\rho_{ab,\min} = 20 \mu\Omega \text{ cm}$, and (c) boundary condition 1 and $\rho_{ab,\min} = 30 \mu\Omega \text{ cm}$. As it

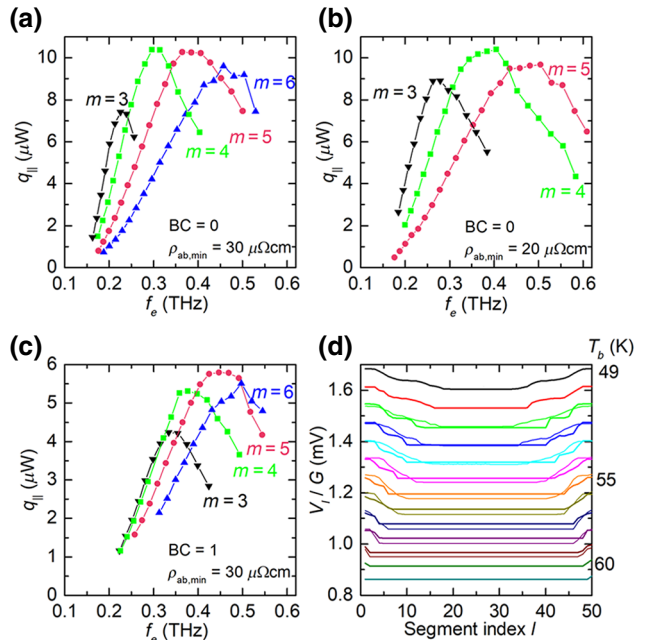


FIG. 9. Power $q_{||}$ vs emission frequency f_e for different resonant modes between $m = 3$ and $m = 6$ and (a) boundary condition 0 and $\rho_{ab,\min} = 30 \mu\Omega \text{ cm}$, (b) boundary condition 0 and $\rho_{ab,\min} = 20 \mu\Omega \text{ cm}$, and (c) boundary condition 1 and $\rho_{ab,\min} = 30 \mu\Omega \text{ cm}$. For the parameters of (c), graph (d) shows V_l/G vs the segment index l . Thick lines are for the $m = 5$ mode, thin lines for the $m = 4$ mode. To obtain the data in (a) to (d) the bath temperature is varied in steps on 1 K. Selected values of T_b are indicated in (d). In (a) the leftmost points are calculated for $T_b = 50$ K ($m = 6$), 51 K ($m = 5$), 55 K ($m = 4$), and 62 K ($m = 3$). In (b) the corresponding values are 47 K ($m = 5$), 48 K ($m = 4$) and 56 K ($m = 3$), and in (c) the leftmost points are calculated at 49 K ($m = 6$ and 5), 51 K ($m = 4$), and 54 K ($m = 3$).

should be expected for a resonance, $q_{||}$ for each mode runs over a maximum as a function of f_e . In all cases the resonances strongly overlap, pointing to a low quality-factor of all modes. This seems to be a real difference to the experimental observation. To resolve the issue one could assume that $\rho_{ab,\min}$ is significantly (at least 1 order of magnitude) higher than expected. Another possibility could be that, for some reason, resonant modes are only excited near their respective maxima.

Let us discuss the different curves in Figs. 9(a)–9(c) in more detail. In all curves the rightmost point in each curve is for the highest bath temperature where a given resonance turned out to be stable. For the subsequent points the bath temperature is decreased in steps of 1 K. In Fig. 9(a) the leftmost points are calculated for $T_b = 50$ K ($m = 6$), 51 K ($m = 5$), 55 K ($m = 4$), and 62 K ($m = 3$). The maxima of the different curves occur at average stack temperatures of 57 K ($m = 6$), 58.5 K ($m = 5$), 62.5 K ($m = 4$), and 66 K ($m = 3$). From the respective values of f_e we calculate mode velocities $c_1 = L f_e / m$ around 4.6×10^7 m/s, which is about 30% lower than the value of 7.1×10^7 m/s found in experiment. From an analytic expression for c_1 [3], which in fact does not take Josephson-vortex formation into account and is derived in the limit $\rho_{ab} \rightarrow \infty$, one would expect that c_1 decreases from 4.4×10^7 m/s to 3.4×10^7 m/s in the temperature range where the maxima in the $m = 3$ –6 modes occur. Thus, the actual values for c_1 observed in simulations are somewhat higher and less temperature dependent than the values of c_1 predicted by the analytic expression. For the data of Fig. 9(b) the corresponding mode velocities are found as $5.5\text{--}6 \times 10^7$ m/s, and for the data of Fig. 9(c) the mode velocities decrease from 6.7×10^7 m/s ($m = 3$) to 5×10^7 m/s ($m = 6$). While some of these numbers approach the experimental value, fine tuning of parameters to make c_1 temperature independent seems to be unnatural. Further hints come from Kakeya *et al.* [34], where also a temperature-independent emission frequency was observed for a stand-alone stack. In their case, highly conducting silver electrodes were affixed to the top and bottom of the stack. This brings, as the authors explain, the sample close to boundary conditions where the in-plane electric field is supposed to vanish at the outermost BSCCO layers and where c_1 is close to c/n , c being the vacuum speed of light and $n \approx 3.4 - 4$ being the diffraction index, see, e.g., Refs. [52,53]. This boundary condition implies that the in-plane currents in the outermost BSCCO electrodes are zero and that c -axis currents in the outermost junctions leave the stack and do not come back, i.e., they are assumed to be dissipated in the contacting metal layers. Our samples have comparatively thin (200 nm) contacting Au layers and in addition there is a substantial contact resistance between the Au layers and the uppermost layers of the BSCCO stack. The boundary conditions we considered reasonably and used in our simulations imply that ac currents either stay confined in the

stack ($BC = 0$) or extend to the contacting Au layer but flow back to the stack. For both cases, the in-plane electric fields and currents are large in the outermost BSCCO layers and c_1 becomes temperature dependent. More work seems to be required to understand the effect of contact resistance and the role of contacting Au layers of intermediate thicknesses.

Finally, in Fig. 9(d) we show the segment-resolved voltage per junction for the $m = 6$ and $m = 5$ modes of Fig. 9(c). Thick lines are for $m = 5$, thin lines for $m = 4$. Like in Fig. 8(b) only the inner segments are locked to the resonance, while voltage across the outer segments is higher. Note that in Fig. 8 the resonances appeared spontaneously while in Fig. 9 they are triggered. Thus, the number of locked segments is in general higher in Fig. 9(d) than in Fig. 8(b). Further note that at a fixed bias the number of locked segments differs for the two modes shown. Thus, if a transition between the two modes would occur, also the excess voltage would change, a feature, which fits to the experimental observations. Perhaps counterintuitively, after a transition the excess voltage, and also the gradient in voltage between locked and unlocked segments, is usually higher than before the transition. Also, the number of locked segments is often lower after the transition. The actual (in)stability criterion for the transition seems to be the magnitude of the in-plane ac currents, which are higher in the state reached after the transition.

V. SUMMARY

In summary, we perform a detailed investigation of THz-emission properties related to resonant cavity modes under different bias conditions. We discuss data for two intrinsic Josephson-junction stacks of the same geometry and a junction number of about 700. The stacks are fabricated, respectively, from an underdoped and an optimally doped BSCCO single crystal. In the low-bias regime, THz emission is found for both stacks. At high bias, in the presence of a hot spot, only the optimally doped stack emitted THz radiation. At high bias, the emission frequency is continuously tunable by changing the bias current and the bath temperature—a feature that also appears in simulations for all cases where high-bias emission is stable. By contrast, at low bias the emission frequencies f_e are remarkably discrete and temperature independent for both stacks. The values of f_e point to the formation of $(0, m)$ cavity modes with $m = 3$ to 6. The total voltage V across the stack varies much stronger than f_e , and there seems to be an excess voltage indicating groups of junctions that are unlocked. In these junctions, the Josephson current seems to oscillate at a higher frequency. For the case of the underdoped stack, we perform intensive numerical simulations based on coupled sine-Gordon equations combined with heat-diffusion equations. Overall features, like the shape of the current-voltage characteristics, the appearance of

(0, m) cavity modes with $m = 3$ to 6, the absence of high-bias emission, the temperature and voltage regions where emission occurs at low bias, or the appearance of an excess voltage, can be reproduced well and point to an unexpected large value of the in-plane resistivity. However, in our simulations the different resonant modes strongly overlap for realistic parameters and the mode velocity is typically temperature dependent and lower than in experiment. The reason for this is presently unclear.

ACKNOWLEDGMENTS

We thank Y. Laplace and A.V. Koshelev for valuable discussions and pointing out Ref. [88]. We gratefully acknowledge financial support by the National Natural Science Foundation of China (Grants No. 61727805, No. 61611130069, No. 61521001, No. 61771235), Jiangsu Key Laboratory of Advanced Techniques for Manipulating Electromagnetic Waves, the Priority Academic Program Development of Jiangsu Higher Education Institutions (PAPD), the RFBR Grant No. 17-52-12051, EU-FP6-COST Action CA16218, the Research Fund of Inonu University, Turkey under Grant Contract No. FUA-2018-1182 and the Deutsche Forschungsgemeinschaft via project KL93013/2.

intrinsic Josephson junction stacks of various geometry, *Phys. Rev. B* **82**, 214506 (2010).

- [7] C. Kurter, L. Ozyuzer, T. Proslie, J. F. Zasadzinski, D. G. Hinks, and K. E. Gray, Counterintuitive consequence of heating in strongly-driven intrinsic junctions of $\text{Bi}_2\text{Sr}_2\text{CaCu}_2\text{O}_{8+\delta}$ mesas, *Phys. Rev. B* **81**, 224518 (2010).
- [8] H. B. Wang, S. Guénon, B. Gross, J. Yuan, Z. G. Jiang, Y. Y. Zhong, M. Grünzweig, A. Iishi, P. H. Wu, T. Hatano, D. Koelle, and R. Kleiner, Coherent Terahertz Emission of Intrinsic Josephson Junction Stacks in the Hot Spot Regime, *Phys. Rev. Lett.* **105**, 057002 (2010).
- [9] M. Tsujimoto, K. Yamaki, K. Deguchi, T. Yamamoto, T. Kashiwagi, H. Minami, M. Tachiki, K. Kadokawa, and R. A. Klemm, Geometrical Resonance Conditions for THz Radiation from the Intrinsic Josephson Junctions in $\text{Bi}_2\text{Sr}_2\text{CaCu}_2\text{O}_{8+\delta}$, *Phys. Rev. Lett.* **105**, 037005 (2010).
- [10] H. Koseoglu, F. Turkoglu, Y. Simsek, and L. Ozyuzer, The fabrication of THz emitting mesas by reactive ion-beam etching of superconducting Bi2212 with multilayer masks, *J. Supercond. Nov. Magn.* **24**, 1083 (2011).
- [11] T. M. Benseman, A. E. Koshelev, K. E. Gray, W. K. Kwok, U. Welp, K. Kadokawa, M. Tachiki, and T. Yamamoto, Tunable terahertz emission from $\text{Bi}_2\text{Sr}_2\text{CaCu}_2\text{O}_{8+\delta}$ mesa devices, *Phys. Rev. B* **84**, 064523 (2011).
- [12] K. Yamaki, M. Tsujimoto, T. Yamamoto, A. Furukawa, T. Kashiwagi, H. Minami, and K. Kadokawa, High-power terahertz electromagnetic wave emission from high- T_c superconducting $\text{Bi}_2\text{Sr}_2\text{CaCu}_2\text{O}_{8+\delta}$ mesa structures, *Opt. Express* **19**, 3193 (2011).
- [13] J. Yuan, M. Y. Li, J. Li, B. Gross, A. Ishii, K. Yamaura, T. Hatano, K. Hirata, E. Takayama-Muromachi, P. H. Wu, D. Koelle, R. Kleiner, and H. B. Wang, Terahertz emission from $\text{Bi}_2\text{Sr}_2\text{CaCu}_2\text{O}_{8+\delta}$ intrinsic Josephson junction stacks with all-superconducting electrodes, *Supercond. Sci. Technol.* **25**, 075015 (2012).
- [14] M. Y. Li, J. Yuan, N. Kinev, J. Li, B. Gross, S. Guénon, A. Ishii, K. Hirata, T. Hatano, D. Koelle, R. Kleiner, V. P. Koshelets, H. B. Wang, and P. H. Wu, Linewidth dependence of coherent terahertz emission from $\text{Bi}_2\text{Sr}_2\text{CaCu}_2\text{O}_8$ intrinsic Josephson junction stacks in the hot-spot regime, *Phys. Rev. B* **86**, 060505(R) (2012).
- [15] I. Kakeya, Y. Omukai, T. Yamamoto, K. Kadokawa, and M. Suzuki, Effect of thermal inhomogeneity for terahertz radiation from intrinsic Josephson junction stacks of $\text{Bi}_2\text{Sr}_2\text{CaCu}_2\text{O}_{8+\delta}$, *Appl. Phys. Lett.* **100**, 242603 (2012).
- [16] T. Kashiwagi, M. Tsujimoto, T. Yamamoto, H. Minami, K. Yamaki, K. Delfanazari, K. Deguchi, N. Orita, T. Koike, R. Nakayama, T. Kitamura, M. Sawamura, S. Hagino, K. Ishida, K. Ivancovic, H. Asai, M. Tachiki, R. A. Klemm, and K. Kadokawa, High temperature superconductor terahertz emitters: Fundamental physics and its applications, *J. J. Appl. Phys.* **51**, 010113 (2012).
- [17] M. Tsujimoto, H. Minami, K. Delfanazari, M. Sawamura, R. Nakayama, T. Kitamura, T. Yamamoto, T. Kashiwagi, T. Hattori, and K. Kadokawa, Terahertz imaging system using high- T_c superconducting oscillation devices, *J. Appl. Phys.* **111**, 123111 (2012).
- [18] M. Tsujimoto, T. Yamamoto, K. Delfanazari, R. Nakayama, T. Kitamura, M. Sawamura, T. Kashiwagi, H. Minami, M. Tachiki, K. Kadokawa, and R. A. Klemm, Broadly

- Tunable Subterahertz Emission from Internal Branches of the Current-voltage Characteristics of Superconducting $\text{Bi}_2\text{Sr}_2\text{CaCu}_2\text{O}_{8+\delta}$ Single Crystals, *Phys. Rev. Lett.* **108**, 107006 (2012).
- [19] F. Turkoglu, H. Koseoglu, Y. Demirhan, L. Ozyuzer, S. Preu, S. Malzer, Y. Simsek, P. Müller, T. Yamamoto, and K. Kadowaki, Interferometer measurements of terahertz waves from $\text{Bi}_2\text{Sr}_2\text{CaCu}_2\text{O}_{8+\delta}$ mesas, *Supercond. Sci. Technol.* **25**, 125004 (2012).
- [20] D. Y. An *et al.*, Terahertz emission and detection both based on high- T_c superconductors: Towards an integrated receiver, *Appl. Phys. Lett.* **102**, 092601 (2013).
- [21] T. M. Benseman, A. E. Koshelev, W. K. Kwok, U. Welp, V. K. Vlasko-Vlasov, K. Kadowaki, H. Minami, and C. Watanabe, Direct imaging of hot spots in $\text{Bi}_2\text{Sr}_2\text{CaCu}_2\text{O}_{8+\delta}$ mesa terahertz sources, *J. Appl. Phys.* **113**, 133902 (2013).
- [22] T. M. Benseman, K. E. Gray, A. E. Koshelev, W. K. Kwok, U. Welp, H. Minami, K. Kadowaki, and T. Yamamoto, Powerful terahertz emission from $\text{Bi}_2\text{Sr}_2\text{CaCu}_2\text{O}_{8+\delta}$ mesa arrays, *Appl. Phys. Lett.* **103**, 022602 (2013).
- [23] S. Sekimoto, C. Watanabe, H. Minami, T. Yamamoto, T. Kashiwagi, R. A. Klemm, and K. Kadowaki, Computed tomography image using sub-terahertz waves generated from a high- T_c superconducting intrinsic Josephson junction oscillator, *Appl. Phys. Lett.* **103**, 182601 (2013).
- [24] H. Minami, C. Watanabe, K. Sato, S. Sekimoto, T. Yamamoto, T. Kashiwagi, R. A. Klemm, and K. Kadowaki, Local SiC photoluminescence evidence of hot spot formation and sub-THz coherent emission from a rectangular $\text{Bi}_2\text{Sr}_2\text{CaCu}_2\text{O}_{8+\delta}$ mesa, *Phys. Rev. B* **89**, 054503 (2014).
- [25] C. Watanabe, H. Minami, T. Yamamoto, T. Kashiwagi, R. A. Klemm, and K. Kadowaki, Spectral investigation of hot spot and cavity resonance effects on the terahertz radiation from high- T_c superconducting $\text{Bi}_2\text{Sr}_2\text{CaCu}_2\text{O}_{8+\delta}$, *J. Phys.: Cond. Mat.* **26**, 172201 (2014).
- [26] M. Ji *et al.*, $\text{Bi}_2\text{Sr}_2\text{CaCu}_2\text{O}_8$ intrinsic Josephson junction stacks with improved cooling: Coherent emission above 1 THz, *Appl. Phys. Lett.* **105**, 122602 (2014).
- [27] M. Tsujimoto, H. Kambara, Y. Maeda, Y. Yoshioka, Y. Nakagawa, and I. Kakeya, Dynamic Control of Temperature Distributions in Stacks of Intrinsic Josephson Junctions in $\text{Bi}_2\text{Sr}_2\text{CaCu}_2\text{O}_{8+\delta}$ for Intense Terahertz Radiation, *Phys. Rev. Appl.* **2**, 044016 (2014).
- [28] T. Kashiwagi, K. Nakade, Y. Saiwai, H. Minami, T. Kitamura, C. Watanabe, K. Ishida, S. Sekimoto, K. Asanuma, T. Yasui, Y. Shibano, M. Tsujimoto, T. Yamamoto, B. Markovic, J. Mirkovic, R. A. Klemm, and K. Kadowaki, Computed tomography image using sub-terahertz waves generated from a high- T_c superconducting intrinsic Josephson junction oscillator, *Appl. Phys. Lett.* **104**, 082603 (2014).
- [29] T. Kashiwagi, K. Nakade, B. Markovic, Y. Saiwai, H. Minami, T. Kitamura, C. Watanabe, K. Ishida, S. Sekimoto, K. Asanuma, T. Yasui, Y. Shibano, M. Tsujimoto, T. Yamamoto, J. Mirkovic, and K. Kadowaki, Reflection type of terahertz imaging system using a high- T_c superconducting oscillator, *Appl. Phys. Lett.* **104**, 022601 (2014).
- [30] T. Kashiwagi, T. Yamamoto, T. Kitamura, K. Asanuma, C. Watanabe, K. Nakade, T. Yasui, Y. Saiwai, Y. Shibano, H. Kubo, K. Sakamoto, T. Katsuragawa, M. Tsujimoto, K. Delfanazari, R. Yoshizaki, H. Minami, R. A. Klemm, and K. Kadowaki, Generation of electromagnetic waves from 0.3 to 1.6 terahertz with a high- T_c superconducting $\text{Bi}_2\text{Sr}_2\text{CaCu}_2\text{O}_{8+\delta}$ intrinsic Josephson junction emitter, *Appl. Phys. Lett.* **106**, 092601 (2015).
- [31] T. Kashiwagi, K. Sakamoto, H. Kubo, Y. Shibano, T. Enomoto, T. Kitamura, K. Asanuma, T. Yasui, C. Watanabe, K. Nakade, Y. Saiwai, T. Katsuragawa, M. Tsujimoto, R. Yoshizaki, T. Yamamoto, H. Minami, R. A. Klemm, and K. Kadowaki, A high- T_c intrinsic Josephson junction emitter tunable from 0.5 to 2.4 terahertz, *Appl. Phys. Lett.* **107**, 082601 (2015).
- [32] T. Kitamura, T. Kashiwagi, T. Yamamoto, M. Tsujimoto, C. Watanabe, K. Ishida, S. Sekimoto, K. Asanuma, T. Yasui, K. Nakade, Y. Shibano, Y. Saiwai, H. Minami, R. A. Klemm, and K. Kadowaki, Broadly tunable, high-power terahertz radiation up to 73 K from a stand-alone $\text{Bi}_2\text{Sr}_2\text{CaCu}_2\text{O}_{8+\delta}$ mesa, *Appl. Phys. Lett.* **104**, 202603 (2014).
- [33] C. Watanabe, H. Minami, T. Kitamura, K. Asanuma, K. Nakade, T. Yasui, Y. Saiwai, Y. Shibano, T. Yamamoto, T. Kashiwagi, R. A. Klemm, and K. Kadowaki, Influence of the local heating position on the terahertz emission power from high- T_c superconducting $\text{Bi}_2\text{Sr}_2\text{CaCu}_2\text{O}_{8+\delta}$ mesas, *Appl. Phys. Lett.* **106**, 042603 (2015).
- [34] I. Kakeya, N. Hirayama, Y. Omukai, and M. Suzuki, Temperature dependence of terahertz emission by an asymmetric intrinsic Josephson junction device, *J. Appl. Phys.* **117**, 043914 (2015).
- [35] X. J. Zhou, J. Yuan, H. Wu, Z. S. Gao, M. Ji, D. Y. An, Y. Huang, F. Rudau, R. Wieland, B. Gross, N. Kinev, J. Li, A. Ishii, T. Hatano, V. P. Koshelets, D. Koelle, R. Kleiner, H. B. Wang, and P. H. Wu, Tuning the Terahertz Emission Power of an Intrinsic Josephson-junction Stack with a Focused Laser Beam, *Phys. Rev. Applied* **3**, 044012 (2015).
- [36] X. J. Zhou, Q. Zhu, M. Ji, D. Y. An, L. Y. Hao, H. C. Sun, S. Ishida, F. Rudau, R. Wieland, J. Li, D. Koelle, H. Eisaki, Y. Yoshida, T. Hatano, R. Kleiner, H. B. Wang, and P. H. Wu, Three-terminal stand-alone superconducting terahertz emitter, *Appl. Phys. Lett.* **107**, 122602 (2015).
- [37] L. Y. Hao *et al.*, Compact Superconducting Terahertz Source Operating in Liquid Nitrogen, *Phys. Rev. Appl.* **3**, 024006 (2015).
- [38] T. Kashiwagi *et al.*, Efficient Fabrication of Intrinsic-Josephson-Junction Terahertz Oscillators with Greatly Reduced Self-heating Effects, *Phys. Rev. Applied* **4**, 054018 (2015).
- [39] T. M. Benseman, A. E. Koshelev, V. Vlasko-Vlasov, Y. Hao, W. K. Kwok, U. Welp, C. Keiser, B. Gross, M. Lange, D. Kolle, R. Kleiner, H. Minami, C. Watanabe, and K. Kadowaki, Current Filamentation in Large $\text{Bi}_2\text{Sr}_2\text{CaCu}_2\text{O}_{8+\delta}$ Mesa Devices Observed via Luminescent and Scanning Laser Thermal Microscopy, *Phys. Rev. Appl.* **3**, 044017 (2015).
- [40] K. Nakade, T. Kashiwagi, Y. Saiwai, H. Minami, T. Yamamoto, R. A. Klemm, and K. Kadowaki, Applications using high- T_c superconducting terahertz emitters, *Sci. Rep.* **6**, 23178 (2016).
- [41] M. Tsujimoto, Y. Maeda, A. Elarabi, Y. Yoshioka, Y. Nakagawa, Y. Wen, T. Doi, H. Saito, and I. Kakeya, Cavity mode

- identification for coherent terahertz emission from high- T_c superconductors, *Opt. Express* **24**, 4591 (2016).
- [42] H. C. Sun *et al.*, Terahertz Spectroscopy of Dilute Gases Using $\text{Bi}_2\text{Sr}_2\text{CaCu}_2\text{O}_{8+\delta}$ Intrinsic Josephson-Junction Stacks, *Phys. Rev. Applied* **8**, 054005 (2017).
- [43] O. Kizilaslan, F. Rudau, R. Wieland, J. S. Hampp, X. J. Zhou, M. Ji, O. Kiselev, N. Kinev, Y. Huang, L. Y. Hao, A. Ishii, M. A. Aksan, T. Hatano, V. P. Koshelets, P. H. Wu, H. B. Wang, D. Koelle, and R. Kleiner, Tuning THz emission properties of $\text{Bi}_2\text{Sr}_2\text{CaCu}_2\text{O}_{8+\delta}$ intrinsic Josephson junction stacks by charge carrier injection, *Supercond. Sci. Technol.* **30**, 034006 (2017).
- [44] M. Tsujimoto, T. Doi, G. Kuwano, A. Elarabi, and I. Kakeya, Engineering and characterization of a packaged high- T_c superconducting terahertz source module, *Supercond. Sci. Technol.* **30**, 064001 (2017).
- [45] Y. Huang *et al.*, Self-mixing Spectra of Terahertz Emitters based on $\text{Bi}_2\text{Sr}_2\text{CaCu}_2\text{O}_{8+\delta}$ Intrinsic Josephson-junction Stacks, *Phys. Rev. Applied* **8**, 054023 (2017).
- [46] A. Elarabi, Y. Yoshioka, M. Tsujimoto, and I. Kakeya, Monolithic Superconducting Emitter of Tunable Circularly Polarized Terahertz Radiation, *Phys. Rev. Applied* **8**, 064034 (2017).
- [47] E. A. Borodianskyi and V. M. Krasnov, Josephson emission with frequency span 1–11 THz from small $\text{Bi}_2\text{Sr}_2\text{CaCu}_2\text{O}_{8+\delta}$ mesa structures, *Nat. Commun.* **8**, 1742 (2017).
- [48] A. Elarabi, Y. Yoshioka, M. Tsujimoto, and I. Kakeya, Circularly polarized terahertz radiation monolithically generated by cylindrical mesas of intrinsic Josephson junctions, *Appl. Phys. Lett.* **113**, 052601 (2018).
- [49] T. Kashiwagi, T. Yuasa, Y. Tanabe, T. Imai, G. Kuwano, R. Ota, K. Nakamura, Y. Ono, Y. Kaneko, M. Tsushima, H. Minami, T. Yamamoto, R. A. Klemm, and K. Kadowaki, Improved excitation mode selectivity of high- T_c superconducting terahertz emitters, *J. Appl. Phys.* **124**, 033901 (2018).
- [50] T. Uchida, W. Kimura, K. Nakajima, T. Tachiki, and T. Uchida, Effect of RF isolation of intrinsic Josephson junctions made of solid Bi-2212 film for terahertz radiation, *IEEE Trans. Appl. Supercond.* **28**, 1800304 (2018).
- [51] L. N. Bulaevskii and A. E. Koshelev, Radiation Due to Josephson Oscillations in Layered Superconductors, *Phys. Rev. Lett.* **99**, 057002 (2007).
- [52] A. E. Koshelev, Alternating dynamic state self-generated by internal resonance in stacks of intrinsic Josephson junctions, *Phys. Rev. B* **78**, 174509 (2008).
- [53] S. Z. Lin and X. Hu, Possible Dynamic States in Inductively Coupled Intrinsic Josephson Junctions of Layered High- T_c Superconductors, *Phys. Rev. Lett.* **100**, 247006 (2008).
- [54] X. Hu and S. Z. Lin, Three-dimensional phase-kink state in a thick stack of Josephson junctions and terahertz radiation, *Phys. Rev. B* **78**, 134510 (2008).
- [55] V. M. Krasnov, Nonlinear Nonequilibrium Quasiparticle Relaxation in Josephson Junctions, *Phys. Rev. Lett.* **103**, 227002 (2009).
- [56] R. A. Klemm and K. Kadowaki, Output from a Josephson stimulated terahertz amplified radiation emitter, *J. Phys. Cond. Mat.* **22**, 375701 (2010).
- [57] M. Tachiki, S. Fukuya, and T. Koyama, Mechanism of Terahertz Electromagnetic Wave Emission from Intrinsic Josephson Junctions, *Phys. Rev. Lett.* **102**, 127002 (2009).
- [58] N. F. Pedersen and S. Madsen, THz generation using fluxon dynamics in high temperature superconductors, *IEEE Trans. Appl. Supercond.* **19**, 726 (2009).
- [59] X. Hu and S. Z. Lin, Cavity phenomena in mesas of cuprate high- T_c superconductors under voltage bias, *Phys. Rev. B* **80**, 064516 (2009).
- [60] T. Koyama, H. Matsumoto, M. Machida, and K. Kadowaki, In-phase electrodynamics and terahertz wave emission in extended intrinsic Josephson junctions, *Phys. Rev. B* **79**, 104522 (2009).
- [61] V. M. Krasnov, Coherent flux-flow emission from stacked Josephson junctions: Nonlocal radiative boundary conditions and the role of geometrical resonances, *Phys. Rev. B* **82**, 134524 (2010).
- [62] A. E. Koshelev, Stability of dynamic coherent states in intrinsic Josephson-junction stacks near internal cavity resonance, *Phys. Rev. B* **82**, 174512 (2010).
- [63] K. Kadowaki, M. Tsujimoto, K. Yamaki, T. Yamamoto, T. Kashiwagi, H. Minami, M. Tachiki, and R. A. Klemm, Evidence for a dual-source mechanism of THz radiation from rectangular mesas of single crystalline $\text{Bi}_2\text{Sr}_2\text{CaCu}_2\text{O}_{8+\delta}$ intrinsic Josephson junctions, *J. Phys. Soc. Jpn.* **79**, 023703 (2010).
- [64] A. A. Yurgens, Temperature distribution in a large $\text{Bi}_2\text{Sr}_2\text{CaCu}_2\text{O}_{8+\delta}$ mesa, *Phys. Rev. B* **83**, 184501 (2011).
- [65] V. M. Krasnov, Terahertz electromagnetic radiation from intrinsic Josephson junctions at zero magnetic field via breather-type self-oscillations, *Phys. Rev. B* **83**, 174517 (2011).
- [66] M. Tachiki, K. Ivanovic, K. Kadowaki, and T. Koyama, Emission of terahertz electromagnetic waves from intrinsic Josephson junction arrays embedded in resonance LCR circuits, *Phys. Rev. B* **83**, 014508 (2011).
- [67] R. A. Klemm, E. R. Laberge, D. R. Morley, T. Kashiwagi, M. Tsujimoto, and K. Kadowaki, Cavity mode waves during terahertz radiation from rectangular $\text{Bi}_2\text{Sr}_2\text{CaCu}_2\text{O}_{8+\delta}$ mesas, *J. Phys. Condens. Matter* **23**, 025701 (2011).
- [68] S. Z. Lin and X. Hu, In-plane dissipation as a possible synchronization mechanism for terahertz radiation from intrinsic Josephson junctions of layered superconductors, *Phys. Rev. B* **86**, 054506 (2012).
- [69] Y. O. Averkov, V. M. Yakovenko, V. A. Yampol'skii, and F. Nori, Terahertz transverse-electric- and transverse-magnetic-polarized waves localized on graphene in photonic crystals, *Phys. Rev. B* **90**, 045415 (2014).
- [70] H. Asai, M. Tachiki, and K. Kadowaki, Three-dimensional numerical analysis of terahertz radiation emitted from intrinsic Josephson junctions with hot spots, *Phys. Rev. B* **85**, 064521 (2012).
- [71] A. Grib and P. Seidel, The influence of standing waves on synchronization and self-heating of Josephson junctions in resonant systems, *Low. Temp. Phys.* **38**, 321 (2012).
- [72] B. Gross, S. Guénon, J. Yuan, M. Y. Li, J. Li, A. Ishii, R. G. Mints, T. Hatano, P. H. Wu, D. Koelle, H. B. Wang, and R. Kleiner, Hot-spot formation in stacks of intrinsic Josephson junctions in $\text{Bi}_2\text{Sr}_2\text{CaCu}_2\text{O}_8$, *Phys. Rev. B* **86**, 094524 (2012).

- [73] B. Gross, J. Yuan, D. Y. An, M. Y. Li, N. Kinev, X. J. Zhou, M. Ji, Y. Huang, T. Hatano, R. G. Mints, V. P. Koshelets, P. H. Wu, H. B. Wang, D. Koelle, and R. Kleiner, Modeling the linewidth dependence of coherent terahertz emission from intrinsic Josephson junction stacks in the hot-spot regime, *Phys. Rev. B* **88**, 014524 (2013).
- [74] F. Liu, S. Z. Lin, and X. Hu, Cavity phenomenon and terahertz radiation of a tall stack of intrinsic Josephson junctions wrapped by a dielectric material, *Supercond. Sci. Technol.* **26**, 025003 (2013).
- [75] H. Asai and S. Kawabata, Intense terahertz emission from intrinsic Josephson junctions by external heat control, *Appl. Phys. Lett.* **101**, 112601 (2014).
- [76] A. Grib and P. Seidel, The influence of external separate heating on the synchronization of Josephson junctions, *Phys. Stat. Solidi B* **251**, 1040 (2014).
- [77] F. Rudau *et al.*, Thermal and electromagnetic properties of $\text{Bi}_2\text{Sr}_2\text{CaCu}_2\text{O}_8$ intrinsic Josephson junction stacks studied via one-dimensional coupled sine-Gordon equations, *Phys. Rev. B* **91**, 104513 (2015).
- [78] F. Rudau, R. Wieland, J. Langer, X. J. Zhou, M. Ji, N. Kinev, L. Y. Hao, Y. Huang, J. Li, P. H. Wu, T. Hatano, V. P. Koshelets, H. B. Wang, D. Koelle, and R. Kleiner, 3D Simulations of the Electrothermal and THz Emission Properties of $\text{Bi}_2\text{Sr}_2\text{CaCu}_2\text{O}_8$ Intrinsic Josephson Junction Stacks, *Phys. Rev. Appl.* **5**, 044017 (2016).
- [79] H. Asai and S. Kawabata, Control of circularly polarized THz wave from intrinsic Josephson junctions by local heating, *Appl. Phys. Lett.* **110**, 132601 (2017).
- [80] D. P. Cerkoney, C. Reid, C. M. Doty, A. Gramajo, T. D. Campbell, M. A. Morales, K. Delfanazari, M. Tsujimoto, T. Kashiwagi, T. Yamamoto, C. Watanabe, H. Minami, K. Kadowaki, and R. A. Klemm, Cavity mode enhancement of terahertz emission from equilateral triangular microstrip antennas of the high- T_c superconductor $\text{Bi}_2\text{Sr}_2\text{CaCu}_2\text{O}_{8+\delta}$, *J. Phys.: Condens. Matter* **29**, 015601 (2017).
- [81] R. A. Klemm, A. E. Davis, and Q. X. Wang, Terahertz emission from thermally managed square intrinsic Josephson junction microstrip antennas, *IEEE J. Sel. Top. Quant. Electron.* **23**, 8501208 (2017).
- [82] R. A. Klemm, A. E. Davis, Q. X. Wang, T. Yamamoto, D. P. Cerkoney, C. Reid, M. L. Koopman, H. Minami, T. Kashiwagi, J. R. Rain, C. M. Doty, M. A. Sedlack, M. A. Morales, C. Watanabe, M. Tsujimoto, K. Delfanazari, and K. Kadowaki, Terahertz emission from the intrinsic Josephson junctions of high-symmetry thermally-managed $\text{Bi}_2\text{Sr}_2\text{CaCu}_2\text{O}_{8+\delta}$ microstrip antennas, *IOP Conf. Ser.: Mater. Sci. Eng.* **279**, 012017 (2017).
- [83] H. C. Sun *et al.*, Compact High- T_c Superconducting Terahertz Emitter Operating up to 86 K, *Phys. Rev. Applied* **10**, 024041 (2018).
- [84] U. Welp, K. Kadowaki, and R. Kleiner, Superconducting emitters of THz radiation, *Nat. Photonics* **7**, 702 (2013).
- [85] I. Kakeya and H. B. Wang, Terahertz-wave emission from Bi2212 intrinsic Josephson junctions: A review on recent progress, *Supercond. Sci. Technol.* **29**, 073001 (2016).
- [86] T. Kashiwagi, H. Kubo, K. Sakamoto, T. Yuasa, Y. Tanabe, C. Watanabe, T. Tanaka, Y. Komori, R. Ota, G. Kuwano, K. Nakamura, T. Katsuragawa, M. Tsujimoto, T. Yamamoto, R. Yoshizaki, H. Minami, K. Kadowaki, and R. A. Klemm, The present status of high- T_c superconducting terahertz emitters, *Supercond. Sci. Technol.* **30**, 074008 (2017).
- [87] R. Kleiner, F. Steinmeyer, G. Kunkel, and P. Müller, Intrinsic Josephson Effect in $\text{Bi}_2\text{Sr}_2\text{CaCu}_2\text{O}_8$ Single Crystals, *Phys. Rev. Lett.* **68**, 2394 (1992).
- [88] J. Corson, J. Orenstein, Sheongshik Oh, J. O'Donnell, and J. N. Eckstein, Nodal Quasiparticle Lifetime in the Superconducting State of $\text{Bi}_2\text{Sr}_2\text{CaCu}_2\text{O}_{8+\delta}$, *Phys. Rev. Lett.* **85**, 2569 (2000).